Building a merged SMOS-SMAP brightness temperatures dataset

Ver.: 1.0 (May 9^{th}, 2023)

Ref.: SO-TN-CB-GS-0109

Équipe Systèmes d'Observation / Micro-ondes Passives

Centre d'Etudes Spatiales de la BIOsphère
18 avenue Edouard Belin – 31401 TOULOUSE – France
☎(+33) 5 6155 8501 – 🖷(+33) 5 6155 8500 – www.cesbio.ups-tlse.fr

Building a merged SMOS-SMAP brightness temperatures dataset

CESBIO-SMOS report **SO-TN-CB-GS-0109**

Remi Madelon[1], Nemesio J. Rodríguez-Fernández[1], Arnaud Mialon[1]

[1] **CESBIO**
UMR 5126 (CNRS, CNES, UPS, IRD, INRAE),
18 av. Edouard Belin, bpi 2801, 31401 Toulouse cedex 9, France

9th May, 2023
Version 1.0

Number of pages: 20

Authors:	Remi Madelon, Nemesio J. Rodríguez-Fernández, Arnaud Mialon		
Circulation:	CESBIO, CNES		
Release	Date	Details	Editors
1	9th May 2023	First version	RM

For any clarifications please contact N. Rodríguez-Fernández (nemesio.rodriguez@cesbio.cnes.fr).

Contents

List of Figures

List of Tables

Abstract

Building climate data records of soil moisture (SM) requires computing long time series by merging retrievals from sensors on-board different satellites, which implies to perform a bias-correction or scaling on the original time series. Due to their long time span and high temporal frequency, model data are mostly used as a common reference for the scaling. However, avoiding model dependency in observational climate data records is needed for some applications. The best alternative would be to use L-band retrievals from the two instruments specifically designed to measure SM, on-board SMOS and SMAP. In addition, the conception of a merged L-band dataset as reference for the scaling should be considered to benefit from both SMAP and SMOS advantages. The most straight forward option would be to apply the same physical-based algorithm to the SMOS and SMAP brightness temperatures (BT) after bias-correction. In this study, different approaches to merge the SMOS and SMAP BT into a common dataset are evaluated, including linear regression, neural networks and CDF-matching. It was found that the best merging approach consists in performing a multi-linear regression at a pixel level using the SMOS BT at 32.5, 37.5 and 42.5 incidence angles as inputs and the SMAP BT as targets. After scaling, the bias between the SMOS and SMAP BT time series is entirely removed, the standard deviation of the difference significantly decreases and the correlation increases in Europe, North Africa and Asia.

1 Introduction

Soil moisture (SM) interacts in many hydrological processes such as infiltration, runoff, precipitation and evaporation Koster et al. (2004), and SM estimates are needed in weather forecasting Drusch (2007); De Rosnay et al. (2013); Rodríguez-Fernández et al. (2016), agriculture applications Guerif and Duke (2000) and to monitor extreme climate events such as floods and droughts Keyantash and Dracup; Jung et al. (2010); Brocca et al. (2010); Lievens et al. (2015); Lopez et al. (2020). This is the reason why SM was identified as one of the 50 "Essential Climate Variables" (ECV) by the Global Climate Observing System (GCOS) in the context of the United Nations Framework Convention on Climate Change (UNFCCC) GCOS (2015).

Long time series of soil moisture (SM) are crucial to monitor the Earth's climate evolution. Although remote sensing from space allows a global monitoring of SM, merging data from different instruments is required due to the relatively short operational life of space missions. To effectively detect SM trends and changes, it is crucial to benefit from the longest time series possible because natural short-term variations can hide the longer ones.

The strategy developed by the European Space Agency (ESA) Climate Change Initiative (CCI) program consists in providing a global SM dataset by combining active and passive measurements from different sensors on-board different satellites (Liu et al., 2011; Dorigo et al., 2012, 2014; Plummer et al., 2017; Dorigo et al., 2017; Gruber et al., 2019; Preimesberger et al., 2021). Since sensors have different characteristics (frequency, spatial resolution, temporal and spatial coverage, polarisation, revisit time, etc.), it is required to perform a bias-correction or scaling on the time series to provide a consistent merged dataset. Modelled surface SM data derived from the Global Land Data Assimilation System (GLDAS, Rodell et al. (2004)) 2.1 Noah are currently used as the scaling reference to bring active and passive microwave data into the same dynamic range. This obviously imposes some of the characteristics of the land surface model (e.g. the absolute values and range) onto the ESA CCI SM merged dataset.

However, observational climate data records (CDR), such as the ESA CCI SM merged dataset, are needed to evaluate modeled CDR and to perform data assimilation into models **??**. Therefore,

observational CDR should be as independent to models as possible. In addition, the growing need for model-free observational CDR of ECV, in particular for SM, is discussed in Dorigo et al. (2017) and in the ESA SM CCI User Requirement Document, which summarizes the ESA CCI SM users requirements surveys.

In the framework of the ESA Support to Science Element Soil Moisture and Ocean Salinity (SMOS) and Advanced Microwave Scanning Radiometer for EOS (AMSR-E) fusion project (Rodríguez-Fernández et al., 2016; Van der Schalie et al., 2018), it was proposed to use L-band instruments such as those from SMOS to produce the SM scaling reference dataset. This was further studied in the framework of the visiting scientist activity of Maria Piles (U. Valencia) taking place from 01/01/2017 to 13/11/2018 (Piles et al., 2018). Then, Madelon et al. (2022) conducted a scaling experiment on the Advanced Microwave Scanning Radiometer 2 (AMSR2) data using several SMOS and Soil Moisture Active and Passive (SMAP) datasets as well as GLDAS as references for the scaling. They actually showed that some SMAP and SMOS products could be good candidates to be used as reference instead of GLDAS. Actually, the best trade-off would be using a merged L-band dataset as reference for the scaling to benefit from both SMAP and SMOS advantages. The most straightforward option would be to apply the same physical-based algorithm such as the Land Parameter Retrieval Model (LPRM, Van der Schalie et al. (2016, 2017)) algorithm to the SMOS and SMAP brightness temperatures (BT) after bias-correction.

In this study, different approaches to build a merged SMOS-SMAP BT dataset are evaluated. Linear regression, neural networks and CDF-matching were tested as scaling methods to effectively remove bias between BT time series, and their respective performances were then compared.

The report is structured as follows. Section 2 presents the different SMOS and SMAP data that were used in this study. Section 3 describes the different scaling methods tested to merge the BT time series. Section 4 shows the performances of each method and section 5 discusses some characteristics of the most promising one. Finally, Section 6 draws the conclusions of this study.

2 Data

2.1 SMOS brightness temperatures

The SMOS satellite was launched on 2 November 2009 by the ESA (Kerr et al., 2010) and carries a passive interferometric radiometer operating at L-band (21 cm, 1.4 GHz) with a spatial resolution of 25-50 depending on the position on the field of view (43 km on average). SMOS ascending and descending orbits cross the equator at 6:00 am and 6:00 pm respectively, and the maximum revisit period is 3 days. The CATDS SMOS L3 V7 BT product was used in this study. It is a multi-orbit product provided by the Centre Aval de Traitement des Données (CATDS) with a grid resolution of 25 km (Al Bitar et al., 2017). BT values are provided in horizontal (H), vertical (V), and Stokes 3 and 4 polarisations for 15 angle bins (each bin 5-degrees wide), centered on angles 2.5° to 62.5°. Note that bin 9 is centered on 40° and has a width of 2 degrees rather than 5°.

2.2 SMAP brightness temperatures

The SMAP satellite was launched on 31 January 2015 by the National Aeronautics and Space Administration (NASA). It carries on board a passive radiometer operating at 1.4 GHz (L-band), and a SAR (active instrument) operating at 1.2 GHz (Entekhabi et al., 2014). The respective spatial resolutions of the two instruments are 40 km and 1 to 3 km, however the radar stopped working a few months after launch. SMAP ascending and descending orbits cross the equator at 6:00 pm and 6:00 am respectively, and the maximum revisit period is 3 days. The SMAP L3 V6 SM product was used in this study. It provides passive measurements of BT at 36-km resolution in H and V polarisations for a fixed incidence angle of 40° degrees (O'Neill et al., 2018, 2019).

3 Methodology

3.1 Data filtering

In this study, SMOS and SMAP BT were filtered as follows.

(*i*) SMAP BT observations for which at least one of the binary flags below is set to 0 were filtered out (see document Chan (2019) for a complete specification of the product content):

- Observation has acceptable quality
- Observation within physical range
- RFI was not detected in the observation
- RFI was not detected corrected in the observation
- Observation had acceptable NEDT
- Observation was a valid value
- Observation was free of RFI

(*ii*) SMOS BT observations of lower quality can be filtered out by using the two following ratios:

- *the* $\frac{Pixel\_BT\_Standard\_Deviation}{Pixel\_Radiometric\_Accuracy}$ ratio, which is an indicator of spurious effects, including RFI. It is specific for each angle bin.
- *the* $\frac{Nb\_RFI\_Flags}{Nviews}$ ratio, which is an indicator of the level of RFI contamination. It is common for all the angle bins.

BT observations for which $\frac{Pixel\_BT\_Standard\_Deviation}{Pixel\_Radiometric\_Accuracy}$ and $\frac{Nb\_RFI\_Flags}{Nviews}$ exceed 1.8 and 0.8 were discarded only if they represent less than 10% of the data within a time series. Otherwise, only the $\frac{Standard\_Dev}{Pixel\_Radio\_Accuracy}$ ratio was used to filter out the data (Mialon et al., 2022).

3.2 Bias-correction methods

To merge the SMOS and SMAP BT time series in a consistent way, it has been chosen to scale, in a statistical sense, a dataset against the other. While SMAP only provides BT at 40 degrees incidence angle, SMOS has the advantage to provide BT at different incidence angles (see sect 2.1). Hence, the SMAP BT were used as the reference for the scaling and the SMOS BT were interpolated from 25-km to 36-km resolution using the closest neighbour approach.

Three types of scaling method were evaluated in this study: (single/multi) linear regression, neural networks and CDF-matching. In all cases, the SMOS BT from the ascending (descending) orbits were scaled against the SMAP BT from the descending (ascending) orbits. For the sake of clarity, only results for the A.M. orbits (ascending SMOS and descending SMAP) in H polarisation are presented in the following sections. The performances of each scaling method are quite the same regardless the orbits and the polarisation used. Also note that only SMOS and SMAP BT from February 2015 to December 2020 were considered in this study.

Table 1 summaries the scaling methods that were tested and whether they were applied at a global scale or at a pixel level.

Table 1: Scaling methods that were tested to merge the SMOS and SMAP BT time series.

Label	Method	Inputs	Targets	Applied at
R1	Linear regression	SMOS BT at 40°	SMAP BT at 40°	Global scale
R2	Linear regression	SMOS BT at 40°	SMAP BT at 40°	Pixel level
R3	Linear regression	SMOS BT at 32.5°, 37.5° and 42.5°	SMAP BT at 40°	Global scale
R4	Linear regression	SMOS BT at 32.5°, 37.5° and 42.5°	SMAP BT at 40°	Pixel level
C1	CDF-matching	SMOS BT at 40°	SMAP BT at 40°	Pixel level
N1	Neural network	SMOS BT at 40°	SMAP BT at 40°	Global scale
N2	Neural network	SMOS BT at 32.5°, 37.5° and 42.5°	SMAP BT at 40°	Global scale

The CDF-matching chosen here is the one proposed in Brocca et al. (2011) and uses a linear fit to find the relationships between the source and the reference data CDF. Firstly, the source and reference CDF are computed with a number of percentiles equal to the number of SM observations in their respective time series. Secondly, the source CDF is linearly interpolated on the percentiles of the reference CDF and the difference between the two is computed. Then, the difference is plotted against the interpolated source CDF and a linear fit is performed. Lastly, the linear fit is used to compute the correction to apply to the source data. This process is repeated independently for each month of the year. As mentioned in Aires et al. (2019), this method has the advantage to provide a continuous transformation but it is more complex to control. Indeed, it can be subjected to instabilities and extreme events are not sure to be well preserved. In the case there was less than 15 percentiles in the reference CDF, the data were not scaled and were discarded.

As shown in table 1, feed-forward neural networks were also tested to scale the SMOS BT on the SMAP ones. They were trained with 5 hidden-layers and roughly 4 millions of observations (10% of the total of observations available from 2015 to 2020 after filtering).

Note that the SMAP L3 product provides two sets of BT values: one with water body correction and the other without. Both sets were independently tested as targets for each method in table 1.

3.3 Evaluation metrics

The goal of the scaling is to improve the agreement between the SMOS and SMAP BT time series. In this study, the agreement before and after scaling is evaluated through three statistical metrics:

- The Pearson correlation (R) between the SMOS and SMAP BT time series.
- The mean difference between the SMOS and SMAP BT time series, or bias, in °K.
- The standard deviation of the difference (STDD) between the SMOS and SMAP BT time series, in °K.

After scaling, the primary objective is to reach a bias the closest possible to 0 °K. The secondary objectives are to reduce the STDD and to increase the correlation (if possible).

4 Results

Figure 1 shows the bias between the SMOS and SMAP BT before and after bias-correction using seven scaling methods (see table 1). It can be observed that the bias between the SMOS and SMAP BT differs across the globe (Fig. 1.A) and that a single global linear transformation is not sufficient to remove it at a pixel level (Fig. 1.R1 and 1.R3). When a specific linear regression is applied for each pixel, the bias is removed with the same order of magnitude whether one or several SMOS incidence angles are used (Fig. 1.R2 and 1.R4). Panel C1 in Figure 1 shows that scaling by CDF-matching at a pixel level is significantly more efficient than applying a global linear regression. However, this technique does not outperform the single and multi linear regression when they are applied at a pixel level (Fig. 1.R2 and 1.R4). The remaining bias after scaling using neural networks (Fig. 1.N1 and 1.N2) are quite comparable to those obtained after applying a global linear regression (Fig. 1.R1 and 1.R3). It implies that introducing non-linearity into the scaling does not improve the bias-removal between the SMOS and SMAP BT time series. Actually, it can be observed that the bias is stronger after scaling using N1 and N2 than using R1 and R3 in some regions such as in Amazonia, Congo or India.

Figure 2 shows the STDD between the SMOS and SMAP BT before and after bias-correction using the seven scaling methods (see table 1). It can be observed that the STDD is higher in the regions the most affected by Radio Frequency Interference (RFI, Fig. 2.A). Comparing panels R1 against R3 and R2 against R4, it can be seen that the STDD decreases more when the linear regression is applied at a pixel level than at a global scale. In addition, comparing panels R2 against R4, the decrease is even more significant when using 3 incidence angles for the regression. The same conclusion is also observed while using neural networks for the scaling (Fig. 2.N1-N2). Scaling using R1 and N1 does not significantly reduce the STDD between the SMOS and SMAP BT time series (Fig. 2.A and Fig. 2.R1-N1). Scaling using R2, R3, C1 or N2 is more efficient and all these four methods are quite comparable. The lowest STDD after scaling are definitively obtained using R4 (Fig. 2.R4).

Figure 3 shows the correlation (R) between the SMOS and SMAP BT before and after bias-correction using the seven scaling methods (see table 1). Overall, the SMOS and SMAP BT times

series are in very good agreement both before and after scaling. The correlation does not change when applying a linear regression or a neural network using only one incidence angle as input (Fig. 1.A and 1.R1-R2-N1). However, the correlation increases a bit in North Africa, Europe and Asia when using 3 incidence angles (Fig. 1.R3-R4-N2). It is interesting to note that these 3 methods are comparable and that the performances do not change whether the regression is performed locally or globally. The correlation obtained after CDF-matching (Fig. 1.C1) is also similar to those obtained after scaling using R3, R4 and N2.

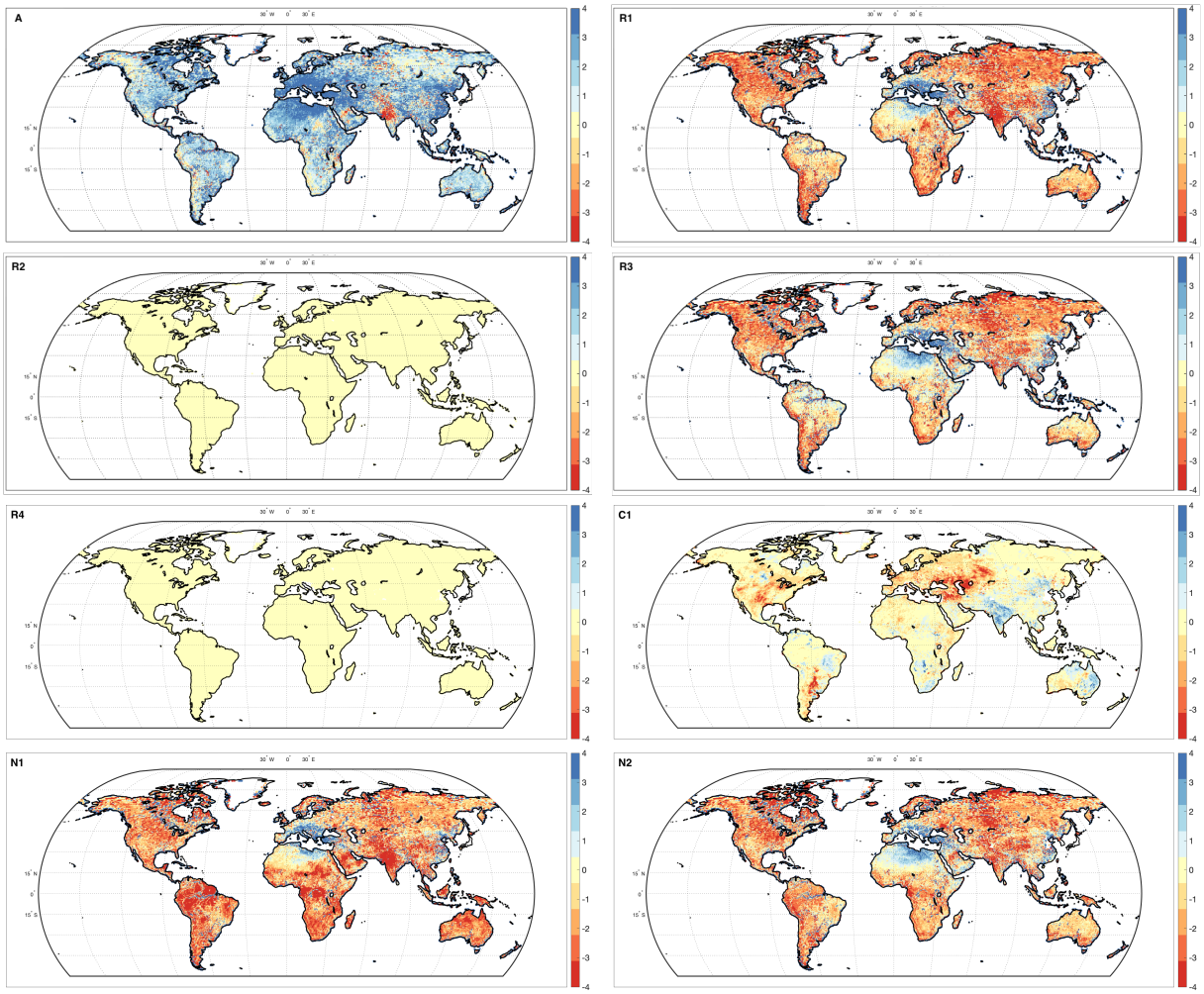

Figure 1: Bias in °K between the SMOS and SMAP BT before bias-correction (**panel A**), and after bias-correction using one of the scaling methods listed in table 1. **Panels R1-2-3-4** show the results obtained with the linear regressions, **panel C1** with the CDF-matching and **panels N1-2** with the neural networks. The metric computation only takes into account the SMOS and SMAP BT data without water body correction in H polarisation from 2015 to 2020 during A.M. orbits.

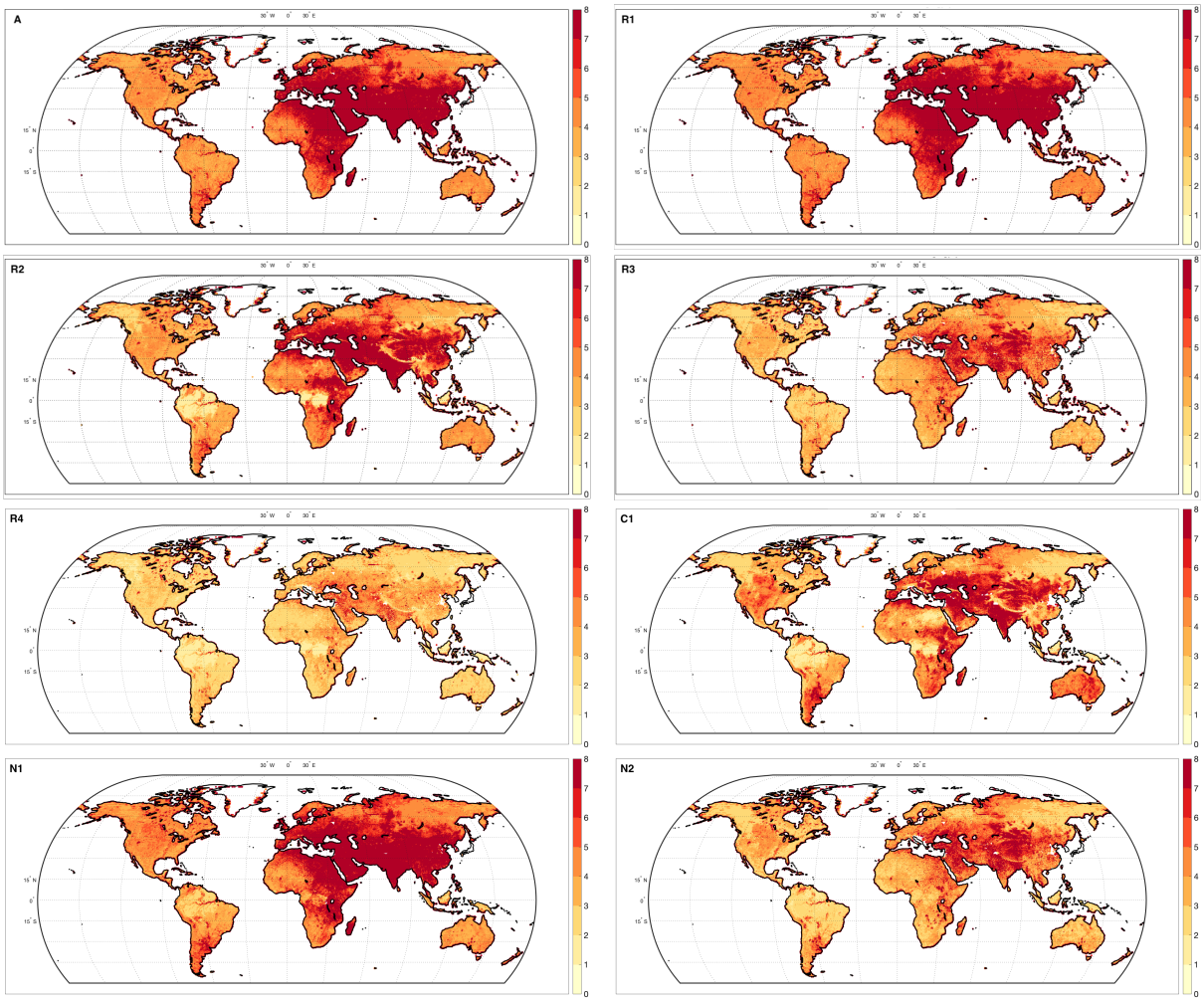

Figure 2: STDD in °K between the SMOS and SMAP BT before bias-correction (**panel A**), and after bias-correction using one of the scaling methods listed in table 1. **Panels R1-2-3-4** show the results obtained with the linear regressions, **panel C1** with the CDF-matching and **panels N1-2** with the neural networks. The metric computation only takes into account the SMOS and SMAP BT data without water body correction in H polarisation from 2015 to 2020 during A.M. orbits.

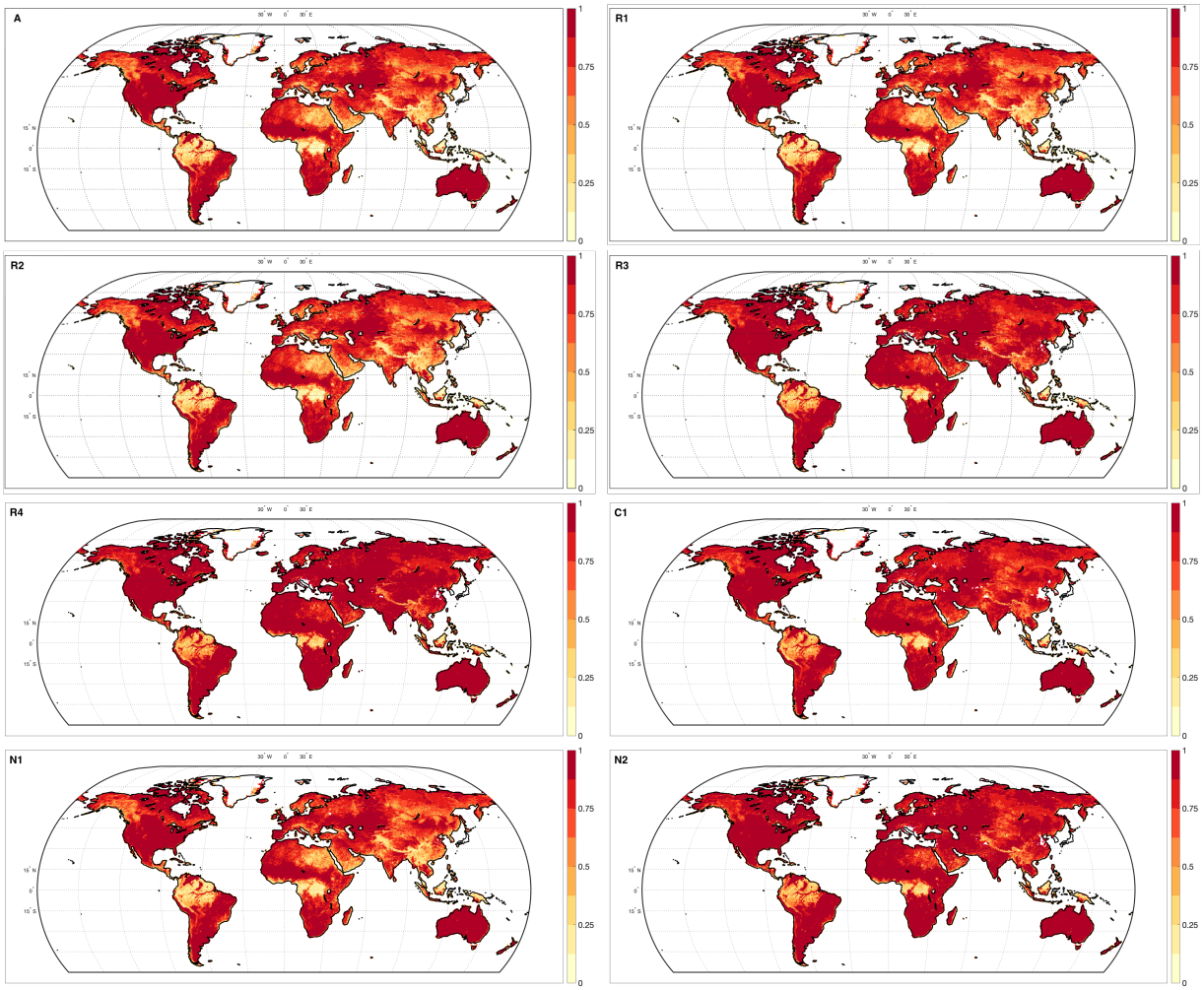

Figure 3: R between the SMOS and SMAP BT before bias-correction (**panel A**), and after bias-correction using one of the scaling methods listed in table 1. **Panels R1-2-3-4** show the results obtained with the linear regressions, **panel C1** with the CDF-matching and **panels N1-2** with the neural networks. The metric computation only takes into account the SMOS and SMAP BT data without water body correction in H polarisation from 2015 to 2020 during A.M. orbits.

5 Discussion

From Figures 1, 2, 3, the best agreement between the SMOS and SMAP BT, in terms of bias, STDD and R, is obtained when the scaling is performed using a linear regression at a pixel level with 3 incidence angles (method R4 in table 1). More advanced methods such as neural networks and CDF-matching (N1, N2 and C1 in table 1, respectively) were tested but they do not outperform method R4.

Figure 4 displays the 3 scaling coefficients and the constant that are derived from method R4

for each pixel. Panels a, b and c highlight that all the 3 incidence angles are useful to predict the SMAP BT even if the angle of 37.5 degrees is more important in general. Indeed, the coefficients are mainly non-zero and are in the same order of magnitude ($\sim$ 0.1-0.6). It is also interesting to note that the coefficients are lower and roughly equivalent in regions covered by tropical forests such as in Amazonia, Congo and Indonesia. This was expected since in tropical regions, the values of the SMOS BT are quite similar regardless the incidence angle. The constant of the linear regression is also higher in these regions (panel d), with values close to 250 °K, while it is mainly between -50 and 50 °K almost everywhere else in the world.

In addition, panels e, f, g, and h from figure 4 show how the coefficients change (in term of relative difference in %) when the SMAP BT with water body correction are used as targets for the regression. For all the panels, in most parts of the globe, the relative differences between the coefficients stay below 5%. However, near the coasts, and large lakes such as those in Canada, differences are above 60% and often exceed 100%. From the first row in figure 5, it can be observed that using the SMAP BT with water body correction as targets for the regression does not change the bias between the SMOS and SMAP BT after scaling. Indeed, it is removed whether using the SMAP BT with water body correction or without. However, the STDD increases over pixels that include large lakes such as in Canada (second row in figure 5). R also drops in these areas (third row in figure 5). Theses differences are due to the interpolation (closest neighbor approach) performed to move the SMOS data from their original grid (25-km resolution) to that of the SMAP data (36-km resolution). In some cases, data over SMOS pixels, that do not include areas covered by water, are moved over SMAP pixels that include water bodies (or the opposite way).

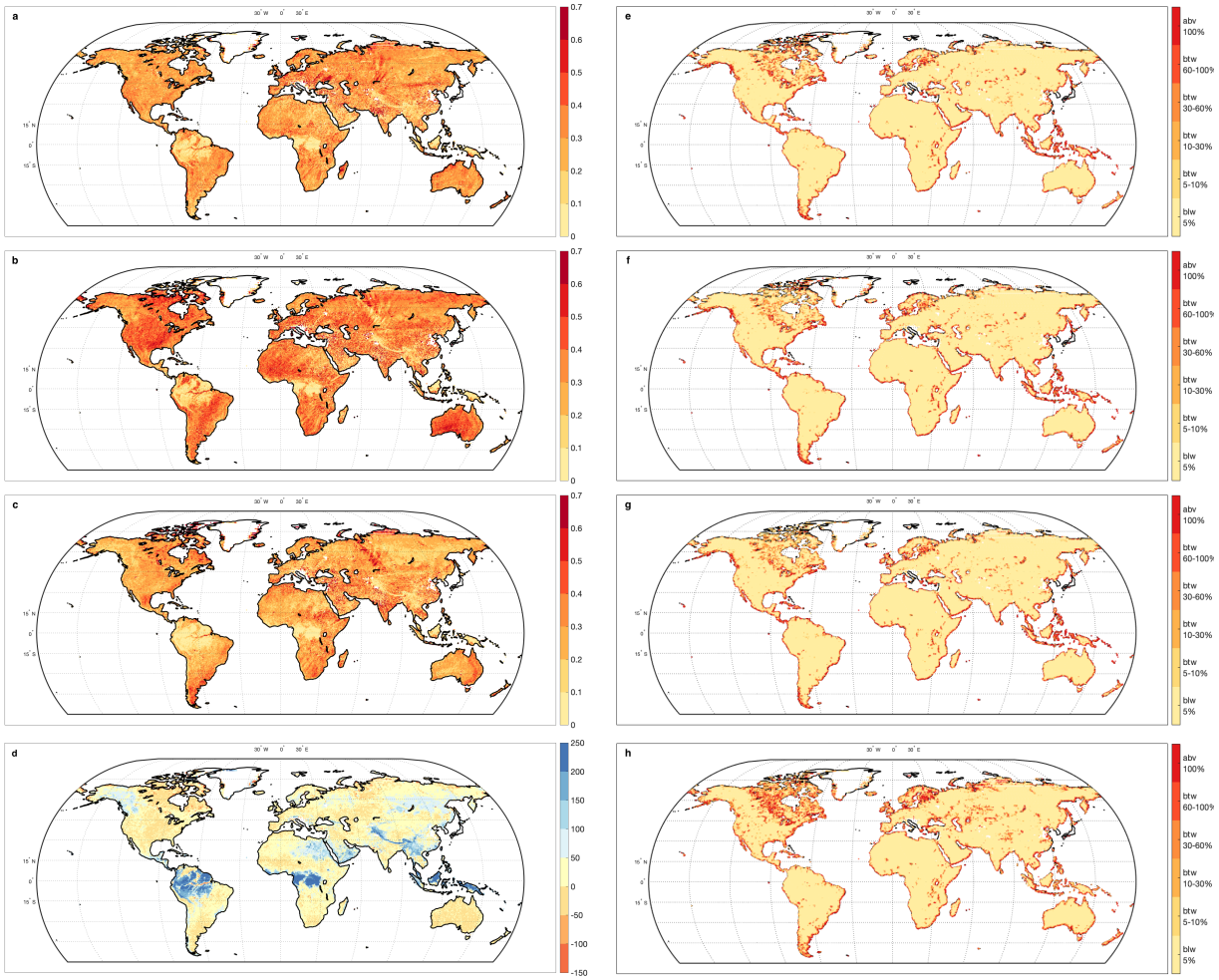

Figure 4: When performing a multi-linear regression at a pixel level to predict the SMAP BT using the SMOS BT at 32.5, 37.5 and 42.5 degrees, three scaling coefficients and a constant are derived per pixel. The **panels a, b, and c** above display the coefficients to apply to the SMOS BT at 32.5, 37.5 and 42.5 degrees, respectively. The **panel d** displays the constant in °K of the linear regression. The linear regression computation only takes into account the SMOS and SMAP BT data without water body correction in H polarisation from 2015 to 2020 during A.M. orbits. **Panels e, f, g, h** compare, in term of relative difference in %, the coefficients from panels a, b, c and d against those obtained when the SMAP BT with water body correction are used as targets for the regression (blw, btw and abv stand for below, between and above, respectively).

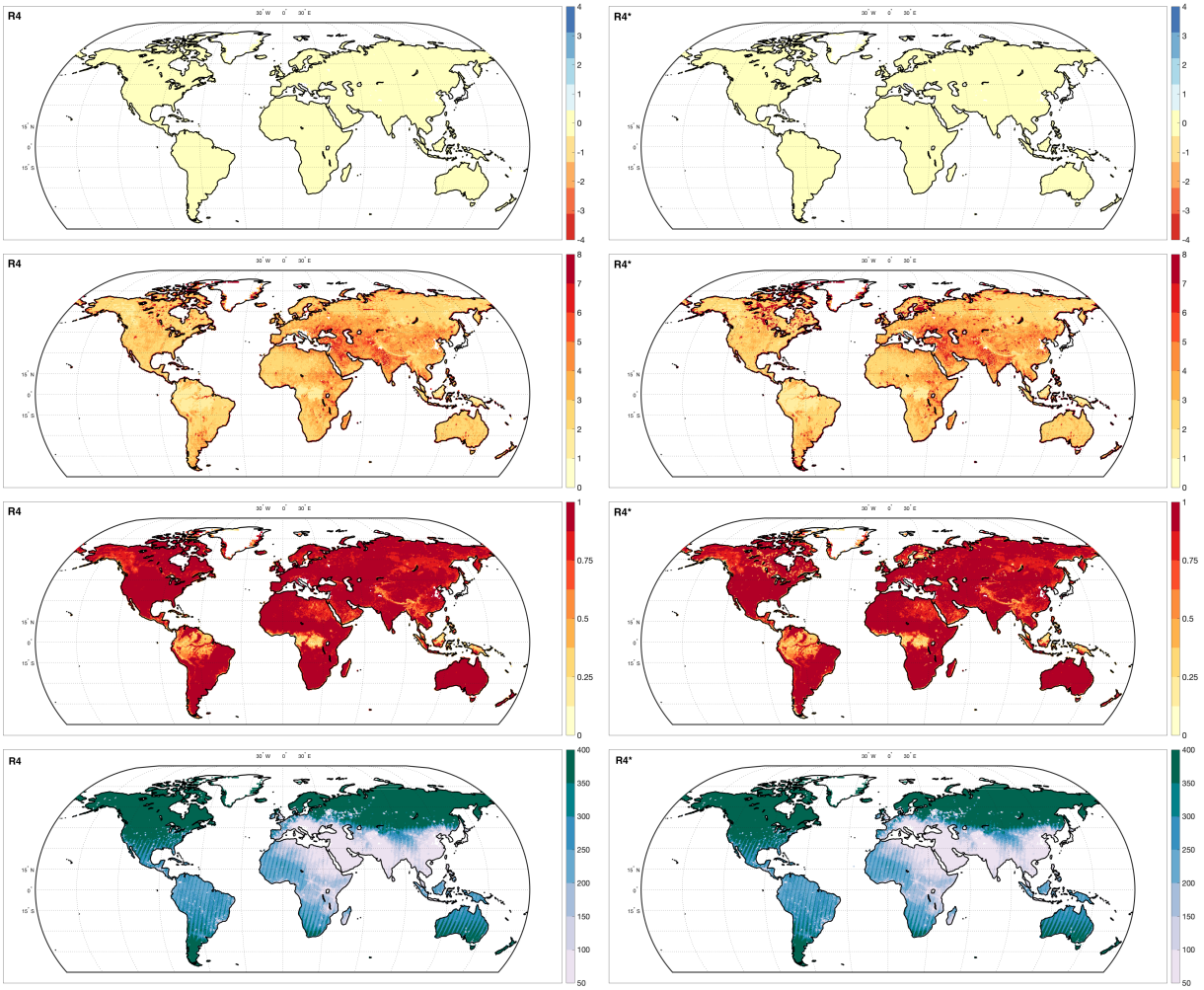

Figure 5: Bias, STDD in °K as well as R between the SMOS and SMAP BT after bias-correction using a multi-linear regression with 3 incidence angles as inputs (R4 in table 1). The first, second and third rows show the bias, STDD and R, respectively. The last row shows the number of observations used to perform the linear regression. The second column displays the metrics when the SMAP BT with water body correction are used as targets (R4*). The metric computation only takes into account the SMOS and SMAP BT in H polarisation from 2015 to 2020 during A.M. orbits.

6 Conclusions

The ESA CCI program provides SM CDR by merging active and passive microwave data from different sensors on-board different satellites. GLDAS is currently used as the reference to scale the different sensor time series in order to remove their relative biases and harmonize their dynamical ranges. Due to a growing need of SM CDR independent of any models from the scientific community, GLDAS is intended to be replaced by an L-band dataset based on the synergistic use of the SMOS

and SMAP measurements. To benefit from advantages of both satellites, one possibility is to build a merged SMOS-SMAP BT dataset and to use it as input to a physical-based algorithm to produce a consistent SM dataset.

In this paper, different scaling methods, such as linear regression, neural networks and CDF-matching, were evaluated to merge the SMOS and SMAP BT time series into a common dataset. The most promising solution is to scale the SMOS BT against the SMAP ones using a multi-linear regression. The transformation is applied at a pixel level using 3 incidence angles as inputs: 32.5, 37.5 and 42.5 degrees.

The next development phase consists in applying the derived scaling coefficients on the SMOS BT from 2010 (SMOS launch date) to 2022, and to merge them with the SMAP BT in a common dataset. Note that the revisit frequency will be higher from 2015 to 2022 because SMOS and SMAP overlap. As the SMAP BT are used as targets, the resulting merged BT dataset will be sampled at 36-km resolution.

Finally, a future study will be dedicated to the evaluation of the SM outputs from the LPRM algorithm using this new merged SMOS-SMAP BT dataset as input.

7 Acknowledgements

This research made use of data from the Centre Aval de Traitement des Données SMOS (CATDS) operated for the Centre National d'Etudes Spatiales (CNES) by The Institut Français de Recherche pour l'Exploitation de la Mer (IFREMER) in France, as well as from the National Snow and Ice Data Center (NSIDC). The authors acknowledge funding from the ESA's Climate Change Initiative for Soil Moisture project and from the Centre National d'Études Spatiales (CNES) APR TOSCA project SMOS-TE. Finally, the authors acknowledge pertinent discussions with Robin van der Schalie, Wolfgang Preimsberger, Pietro Stradiotti and Alexander Grüber in the context of the ESA CCI project for Soil Moisture (Contract No. 4000104814/11/I-NB and 4000112226/14/I-NB).

Bibliography

Aires, F., P. Weston, P. de Rosnay, and D. Fairbairn, 2019: Statistical approaches to assimilate ascat soil moisture information: Part i methodologies and first assessment. *Quarterly Journal of the Royal Meteorological Society*, 2–31.

Al Bitar, A., et al., 2017: The global SMOS level 3 daily soil moisture and brightness temperature maps. *Earth System Science Data*, 9, 293–315.

Brocca, L., F. Melone, T. Moramarco, W. Wagner, V. Naeimi, Z. Bartalis, and S. Hasenauer, 2010: Improving runoff pre- diction through the assimilation of the ascat soil mois- ture product. *Hydrol. Earth Syst. Sci.*, 14, 1881–1893.

Brocca, L., et al., 2011: Soil moisture estimation through ASCAT and AMSR-E sensors: An inter-comparison and validation study across europe. *Remote Sensing of Environment*, 115, 3390–3408.

Chan, S., 2019: Level 3 Passive Soil Moisture Product Specification Document. Tech. Rep. JPL D-72551, JPL, NASA.

De Rosnay, P., M. Drusch, D. Vasiljevic, G. Balsamo, C. Albergel, and L. Isaksen, 2013: A simplified extended kalman filter for the global operational soil moisture analysis at ecmwf. *Quarterly Journal of the Royal Meteorological Society*, 139 (674), 1199–1213.

Dorigo, W., et al., 2014: Evaluation of the esa cci soil moisture product using ground-based observations. *Remote Sensing of Environment*.

Dorigo, W., et al., 2017: Esa cci soil moisture for improved earth system understanding: State-of-the art and future directions. *Remote Sensing of Environment*, 203, 185–215.

Dorigo, W. A., R. A. M. de Jeu, D. Chung, R. M. Parinussa, Y. Y. Liu, W. Wagner, and D. Fernandez-Prieto, 2012: Evaluating global trends (1988-2010) in harmonized multi-satellite surface soil moisture. *Geophysical Research Letters*.

Drusch, M., 2007: Initializing numerical weather prediction models with satellite-derived surface soil moisture: Data assimilation experiments with ECMWF's integrated forecast system and the TMI soil moisture data set. *Journal of Geophysical Research: Atmospheres (1984–2012)*, 112 (D3).

Entekhabi, D., S. Yueh, P. E. O'Neill, and K. H. Kellogg, 2014: SMAP Handbook. Tech. rep., Jet Propulsion Laboratory, NASA.

GCOS, 2015: Status of the global observing system for climate. Tech. rep., Global Climate Observing System, World Meteorological Organization, Report 195.

Gruber, A., T. Scanlon, R. van der Schalie, W. Wagner, and W. Dorigo, 2019: Evolution of the esa cci soil moisture climate data records and their underlying merging methodology. *Earth System Science Data*, 1–37.

Guerif and Duke, 2000: Adjustment procedures of a crop model to the site specific characteristics of soil and crop using remote sensing data assimilation. *Agriculture Ecosystems Environment*, 57–69.

Jung, M., et al., 2010: Recent decline in the global land evapotranspiration trend due to limited moisture supply. *Nature*, 467 (7318), 951–954.

Kerr, Y., et al., 2010: The SMOS mission: New tool for monitoring key elements ofthe global water cycle. *Proceedings of the IEEE*, 98 (5), 666–687.

Keyantash, J. and J. A. Dracup, ????: The quantification of drought: an evaluation of drought indices. *American Meteorologyical Society , year = 2002, volume = 83, pages = 1167–1180,*.

Koster, R. D., et al., 2004: Regions of strong coupling between soil moisture and precipitation. *Science*, 305 (5687), 1138–1140.

Lievens, H., S. Tomer, A. Al Bitar, and et al., 2015: Smos soil moisture assimilation for improved hydrologic simulation in the murray darling basin, australia. *Remote Sensing of Environment*, 168, 146–162.

Liu, Y., R. Parinussa, W. Dorigo, R. De Jeu, W. Wagner, A. van Dijk, M. McCabe, and J. Evans, 2011: Developing an improved soil moisture dataset by blending passive and active microwave satellite-based retrievals. *Hydrology and Earth System Sciences*, 15, 425–436.

Lopez, T., A. Al Bitar, S. Biancamaria, A. Güntner, and A. Jäggi, 2020: On the use of satellite remote sensing to detect floods and droughts at large scales. *Surveys in Geophysics*, 41(6), 1461–1487.

Madelon, R., N. J. Rodríguez-Fernández, R. van der Schalie, T. Scanlon, A. Al Bitar, Y. H. Kerr, R. de Jeu, and W. Dorigo, 2022: Toward the removal of model dependency in soil moisture climate data records by using an l-band scaling reference. *IEEE Journal of Selected Topics in Applied Earth Observations and Remote Sensing*, 15, 831–848.

Mialon, A., F. Cabot, Y. Kerr, N. Rodriguez, and R. Madelon, 2022: Smos level 3 brightness temperature (tb) users'manual and useful tips quality assessment flags. Tech. Rep. SMOS Ground Segment SO-TN-CB-CA-0097, CESBIO, Toulouse, France.

O'Neill, P. E., S. Chan, E. G. Njoku, T. Jackson, and R. Bindlish, 2018: Smap l2 radiometer half-orbit 36 km ease-grid soil moisture, version 5. *NASA National Snow and Ice Data Center Distributed Active Archive Center*.

O'Neill, P. E., S. Chan, E. G. Njoku, T. Jackson, R. Bindlish, and J. Chaubell, 2019: Smap l3 radiometer global daily 36 km ease-grid soil moisture, version 6. *NASA National Snow and Ice Data Center Distributed Active Archive Center*.

Piles, M., R. van der Schalie, A. Gruber, J. Muñoz-Marí, G. Camps-Valls, A. Mateo-Sanchis, W. Dorigo, and R. de Jeu, 2018: Global estimation of soil moisture persistence with l and c-band microwave sensors. 8259–8262.

Plummer, S., P. Lecomte, and M. Doherty, 2017: The esa climate change initiative (cci): A european contribution to the generation of the global climate observing system. *Remote Sensing of Environment*, 203, 2–8.

Preimesberger, W., T. Scanlon, C. H. Su, A. Gruber, and W. Dorigo, 2021: Homogenization of structural breaks in the global esa cci soil moisture multisatellite climate data record. *IEEE Transactions on Geoscience and Remote Sensing*, 59(4), 2845–2862.

Rodell, M., et al., 2004: The global land data assimilation system. *American Meteorological Society*, (24), 381–394.

Rodríguez-Fernández, N. J., et al., 2016: Long term global surface soil moisture fields using an SMOS-trained neural network applied to AMSR-E data. *Remote Sensing*, 8 (11), 959.

Rodríguez-Fernández, N. J., P. de Rosnay, C. Albergel, F. Aires, C. Prigent, Y. H. Richaume, P.and Kerr, and J. Muñoz-Sabater, 2016: SMOS Neural Network Soil Moisture data assimilation. Tech. Rep. ECMWF ESA report, ECMWF, Reading, UK.

Van der Schalie, R., R. De Jeu, R. Parinussa, N. Rodriguez-Fernandez, Y. Kerr, A. Al-Yaari, J.-P. Wigneron, and M. Drusch, 2018: The effect of three different data fusion approaches on the quality of soil moisture retrievals from multiple passive microwave sensors. *Remote Sensing*, 10 (1), 107.

Van der Schalie, R., Y. Kerr, J. Wigneron, N. Rodríguez-Fernández, A. Al-Yaari, and R. de Jeu, 2016: Global SMOS soil moisture retrievals from the land parameter retrieval model. *International Journal of Applied Earth Observation and Geoinformation*, 45, 125–134.

Van der Schalie, R., et al., 2017: The merging of radiative transfer based surface soil moisture data from SMOS and AMSR-E. *Remote Sensing of Environment*, 189, 180–193.